Liquid Metals Hot Paper

International Edition: DOI: 10.1002/anie.201912639
German Edition: DOI: 10.1002/ange.201912639

Chameleon Metals: Autonomous Nano-Texturing and Composition Inversion on Liquid Metals Surfaces

*Andrew Martin[+], Winnie Kiarie[+], Boyce Chang, and Martin Thuo**

Abstract: *Studies on passivating oxides on liquid metals are challenging, in part, due to plasticity, entropic, and technological limitations. In alloys, compositional complexity in the passivating oxide(s) and underlying metal interface exacerbates these challenges. This nanoscale complexity, however, offers an opportunity to engineer the surface of the liquid metal under felicitous choice of processing conditions. We inferred that difference in reactivity, coupled with inherent interface ordering, presages exploitable order and selectivity to autonomously present compositionally biased oxides on the surface of these metals. Besides compositional differences, sequential release of biased (enriched) components, via fractal-like paths, allows for patterned layered surface structures. We, therefore, present a simple thermal-oxidative compositional inversion (TOCI) method to introduce fractal-like structures on the surface of these metals in a controlled (tier, composition, and structure) manner by exploiting underlying stochastic fracturing process. Using a ternary alloy, a three-tiered (in structure and composition) surface structure is demonstrated.*

Introduction

Surface of a material is its dissipation horizon (both mass and energy), hence it plays a critical role in establishing equilibria between otherwise thermodynamically dissimilar (material vs. air) systems.[1] Though limited in total number of atoms, surfaces or interfaces are an ensemble of disparate energy microstates.[2] By necessity, curved surfaces often bear sharp energy and compositional gradients (as captured by interfacial excess, Γ_i, and the Laplace pressure jump condition, ΔP). These gradients, in turn, can dictate energy state(s) of the enclosed bulk. In metal systems, for example, formation of passivating oxides induces both adverse (e.g. non-Newtonian flow,[3] lustre, surface defects, wettability, metastability)[4] and advantageous (e.g. protection, catalysis,[5] redox buffering,[6] and undercooling[7]) properties. These surface oxides can grow to their equilibrium dimensions within milliseconds and passivate depending on the conditions.[8] Oxidation, however, depends on stoichiometry, oxidant diffusion, reduction potential (E^0), microstructure, cohesive energy density, atomic size, temperature, and pressure.[9] In metallic alloys, the complexity of this oxidation process necessitates a kinetics-driven differentiation and in situ self-assembly across a thin (7–30 Å) interface.[2c,d,8a] Selectively engineering this thin, complex, tangential, component(s) of a material is challenging due to entropic domination by the bulk.[2c,d]

In liquid metal alloys, the oxide interface in which this self-limiting oxidation process occur is a complex pseudo-equilibrium system. In oxidizing environment at time, $t = 0$, all elemental components of an alloy can oxidize. This initial stoichiometric dictated oxidation, kinetically self-sorts based on E^0, cohesive energy density, atomic size (hence diffusivity), and oxygen partial pressure.[9c] At $t > 0$, the lowest E^0 element eventually dominates the exterior surface of the metal.[2c,d] For a eutectic (or other stable) alloy mixture, continued oxidation may perturb the bulk equilibrium composition as one (or more) of the components is selectively removed. This compositional change, albeit small, induces an interface accumulation of higher E^0 component(s).[2c,d] Shift from statistical- (at $t = 0$) to E^0 -driven oxidation, coupled with diminished oxidant flux, leads to formation of sub-oxides beneath the oxidized low E^0 component, while the interface phase-segregated components bridge the sub-oxides to the bulk.[10] This self-sorting process leads to a structured, layered interface with sharp composition gradients.[2a,c,d] Such sharp concentration gradients imply that the oxide-bulk metal interface has a high chemical potential gradient, ($\Delta\mu$). An exponential decay in oxide growth is expected[9c, 11] and at a certain critical thickness (d_c^p) passivation occurs.

Akin to the surface of a liquid (shift in Gibbs dividing plane), surface composition changes when these metal–oxide interfaces are thermally perturbed.[2a] Considering that oxygen flux increases with temperature, d_c^p increases with concomitant increase in amount of high E^0 element sub-oxides, and segregated elemental components (Figure 1a). The stochastic increase in diffusion and volumetric change in the surface oxide implies that texturing should occur, with thermal stress leading to fracture and release of the underlying concentration-differentiated layers. The process repeats ad infinitum until the next subsequently E^0 component is significantly depleted or the particle is fully oxidized. It therefore follows that surface of a liquid metal particle can continuously invert its composition under thermal stimuli rendering them "chameleon surfaces". Herein we demonstrate this behavior, and its potential in surface patterning.

Eutectic gallium–indium–tin (galinstan: 68 % Ga, 22 % In, 10 % Sn w/w; m.p. ≈ 11 °C) core–shell particles were synthesized using the SLICE method.[7] The synthesized particles were ca. 1–5 μm in diameter, with a liquid core and a smooth

[*] A. Martin,[+] W. Kiarie,[+] B. Chang, M. Thuo
Department of Materials Science and Engineering
Iowa State University
2220 Hoover Hall, Ames, IA 50011 (USA)
E-mail: mthuo@iastate.edu

[+] These authors contributed equally to this work.

Supporting information and the ORCID identification number(s) for the author(s) of this article can be found under https://doi.org/10.1002/anie.201912639.

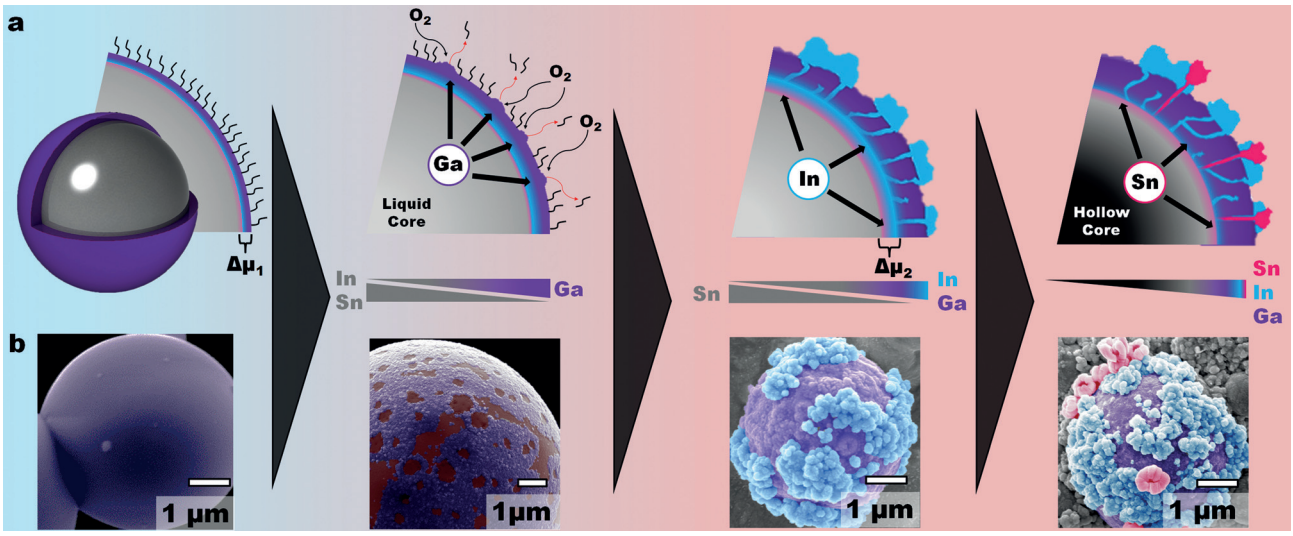

Figure 1. a) Schematic of oxide transformation mechanism for ternary core–shell liquid metal particle. b) SEM image of different oxidation steps correlating with the mechanisms displayed above.

surface oxide stabilized by an acetate ligand (Figure 1b and Figure S1a). For clarity and brevity all particle images are false colored, non-colorized images are given in the SI. These particles were then thermally treated (up to 1273 K) in a Thermogravimetric analysis (TGA) instrument (here used as an oven) under reduced oxygen at 100 K increments.[2a]

Surface morphology change in galinstan particles is visible starting at 573 K (Figure $2a_i$ and Figure S1b). Shape deformations (depressions) are observed at 573 K, likely due to thermal expansion and contraction. Adding isothermal time at this temperature, or raising the temperature to 673 K (Figure S1c), increases the severity of these deformations (Figure $2a_{ii}$ and Figure S1c). Increase in temperature, however, enhances oxygen permeability enabling further oxidation (expansion-induced diffusion-limited oxidation, EDO).[2a] At 773 K surface texture changes are observed (Figure $2b_i$), as a new layer (tier I) starts forming on top of the smooth passivating shell. Some variations of this surface feature exist due to potential thermal gradient and proximity to the pan walls in the TGA (Figure S2a–f). Surface cracks are also observed at high curvature points (Figure $2b_i$ and Figure S2g–l) suggesting that the oxide shell is thick, hence fractures with thermal expansion-contraction. For brevity, this process is referred to as thermo-mechanical fracture leakage and oxidation (TFO).[2a] As expected, holding the particle at 773 K leads to continued growth of tier I to almost complete surface coverage (Figure $2b_{ii}$). Holding the sample at this temperature (isothermal time) also allow the oxide to thicken to a point where it can withstand thermal shock and surface depressions are no longer observed (Figure $2b_{ii}$). Concomitant generation of a new, compositionally different, layer (tier II) occurs on adding isothermal time. This new layer is stochastically distributed throughout the surface of the particles, albeit at low surface coverage (Figure $2b_{ii}$). Increasing the treatment temperature to 873 K leads to rapid growth of the tier II material resulting in surface-grafted nanowires (Figure $2c_i$). Adding isothermal time or increasing the temperature to 973 K leads to a significant decrease in the surface nanowire population and conversion to sintered particle networks (Figure $2c_{ii}$ and S1f). We infer this evolution to be due to sintering of the nanowires, with increased oxidation rate, confirming that the nanowires are a kinetic product—that is, growth rate needs to be higher than the agglomeration/sintering rate.

At 1173 K, onto the tier I covered surface, more tier II forms (Figure $2d_i$). We observe that the texture of tier I is significantly different than that observed at 773 K, with a central depression surrounded by an annular structure (Figure $2d_i$). The grainy structure of these features suggests that they are likely formed from an Ostwald-type ripening of small particles that upon cooling and associated surface changes, contract into these annular structures. A similar grainy structure and sintering of spherical units is also observed for tier II but without the annular structure (Figure $2d_i$). When the particles are held at 1173 K for $\geq$ 30 minutes, new compositionally different features are observed (tier III). These new features have a central crater surrounded by petal-like structures (Figure $2d_{ii}$). Tier III grows on top of either tier I or II, although significant localization around tier II is observed. This selective distribution leads us to infer that tier II may be associated with the generation of the compositionally different layers from which tier III emanates. This inference is in line with TFO and the ansatz that selective (E^0-driven) oxidation of an alloy surface leads interfacial enrichment of the lesser reactive component. This enrichment should manifest in the composition of the resulting oxides when selectively released. To confirm this observation, in a 3-component alloy, further oxidation after formation of tier III should lead to complete solidification of the particle as no other element can be released.

Energy dispersive X-ray spectroscopy (EDS) analysis of the surface of the three-tiered particle, revealed the hypothesized compositional asymmetry in the tiers and across the structure of the fully oxidized particle (Figure 3). A compositional map of a full particle shows complimentary distribution in the three components making up the alloy (Figure 3a). Tier

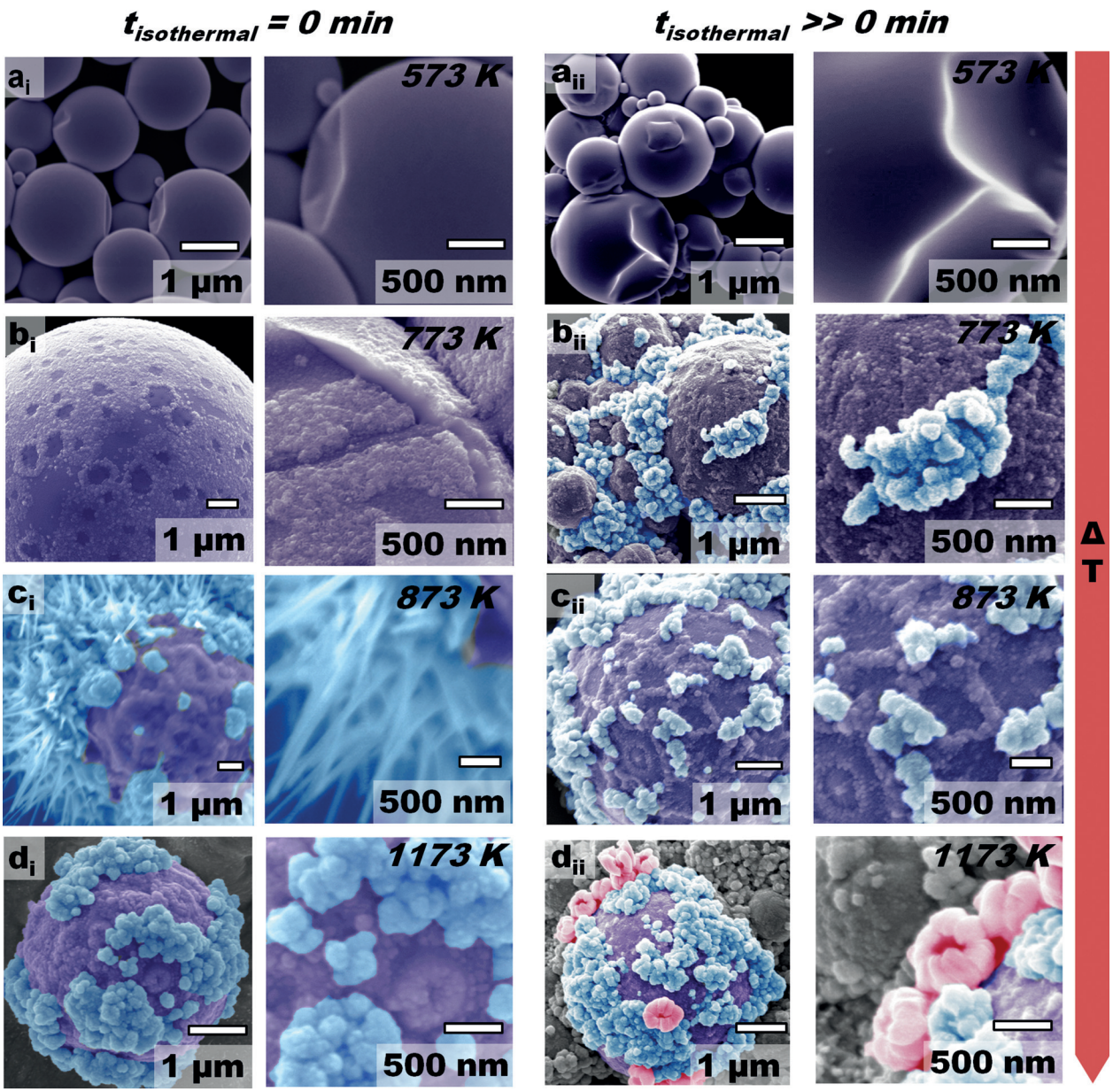

Figure 2. Micrograph of GaInSn particles heat treated for with (ii) and without(i) isothermal time at peak temperature. For column ii isothermal times were:(a_{ii}) 30 minutes, (b_{ii}) 45 minutes, (c_{ii}) 30 minutes and (d_{ii}) 60 minutes at a) 573 K, b) 773 K, c) 873 K and d) 1173 K. With false coloring in high-magnification images highlighting the different tiers of surface texture modification. For clarity gallium- (purple), indium- (blue), and tin- (pink) rich regions are highlighted.

I is gallium-rich, tier II is largely indium, while tier III is enriched in tin (Figure 3b). Each major element makes up ≈70% of the metals in their respective tier. We observe that the non-major components are ≈5–20 atomic %. The lowest E^0 component, Ga, decreases with increase in tier level while highest E^0, Sn, has an inverse progression (Figure 3b). Indium, with an E^0 between Ga and Sn, has a maxima in tier II (Figure 3b). The correlation between tier level and progression in E^0 suggests that the tier are associated with interfacial phase segregation, hence TFO. Previously,[2a] analogous EDS analysis was compared to surface-sensitive Auger and XPS (X-ray photoelectron spectroscopy) with good agreement. We, therefore, similarly infer that the EDS data is representative of surface differences. To further support the ansatz on gradients in interface composition, we analyzed distribution of the three components across the diameter of a particle that had been heated at 1173 K for 60 minutes (fully oxidized). We anticipated, and confirmed, that this treatment would lead to complete oxidation of the particle, hence solidification, allowing us to section it using FIB (focused ion beam). Figure 3c shows a cross-section of such a particle with the associated EDS elemental maps. The core of the particle is Sn-rich, even though Sn is only 10% of the starting alloy. Progression in composition mirrors that of decreasing surface tier levels, that is; the core is Sn rich while the surface is Ga-rich with In enriching an intermediate

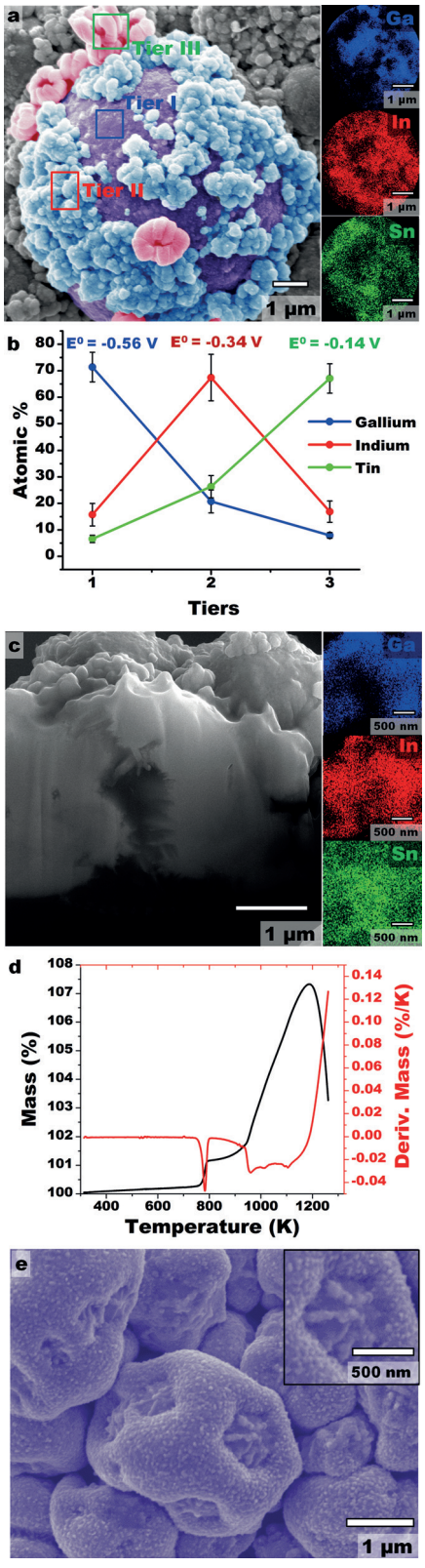

Figure 3. Composition analysis: a) EDS map of GaInSn particle heat treated for 60 minutes at 1173 K. b) Concentration average of heat-treated particle shown in (a), separated in 3 different tiers. c) Cross sectional EDS Map of particle treated at 1173 K. d) TGA curve of heat-treated galinstan particles. e) SEM micrograph of particle heated to 1273 K.

section. We therefore infer that the surface texturing is a thermal-oxidative compositional inversion (TOCI) process governed by reduction potential, and concomitant interfacial enrichment immediately below the passivating oxide shell.

To further confirm the sequential nature of this oxidation driven surface composition inversion, we analyzed mass changes with increase in temperature (Figure 3d). Based on previous studies,[12] we anticipate that the acetate ligand will desorb before the formation of tier 1. An initial slow, but gradual increase in mass is observed on the thermogram. A sharp increase in mass is observed at 773 K which coincides with appearance of tier II. A second mass increase is observed from 993 K (tier III) but this drops at ca. 1273 K. A gradual loss in mass is observed beyond this temperature, which confirms that all possible oxidation is achieved and either volatilization of the lowest vapor pressure component is occurring or this could be due to degradation of the oxide. As a control, we repeat this measurements under inert atmosphere and observe no significant change in mass (Figure S4) indicating that the gain in mass is due to oxidation. We observe that particle morphology changes with some of the more prominent features varnishing, and the particles volumetrically shrink, in agreement with the mass loss (Figure 3e). Based on the stepwise TFO surface texture evolution, we hypothesized that exploitation of surface fracture patterns of the thickening oxide can lead to controlled growth of fractal-like patterns on the surface of the particles.

Fractal-like growth of metal oxide surface structure has been demonstrated via deposition.[13] Autonomous compositional tunable growth of such oxides has, however, not been reported. From the discussion above, we infer that such patterning can be accomplished using TOCI albeit under felicitous choice of reaction conditions. Since our approach is based on fracture patterns across the passivating oxide layer, we anticipate that the patterns will highly depend on alloy composition and oxide thickness. Since galinstan forms a predominantly gallium oxide shell, we demonstrate this fractal-like patterning using Ga-based alloys. A focus on Ga limits this investigation to tier I only.

Figure 4 summarizes the fractal-like growth of tier I oxide on Ga-based unary (Figure 4a), binary (Figure 4b), and ternary (Figure 4c and d) systems. Thermal treatment of Ga particles to 773 K leads to wide fractal-like patterns on the surface (Figure 4a). For a binary alloy, eutectic gallium indium (EGaIn, 75.5% Ga, 24.5% In w/w), also treated to 773 K, the fractal patterns are wider than in the unary albeit not containing as much material (not as dense). Extending this to the ternary galinstan alloy, fractal-like patterns are formed across the surface as fused agglomeration of smaller particles (Figure 4d). To further tune the oxidation on the ternary, particles treated at a slightly lower temperature (673 K) showed web-like fractals (Figure 4c). We can therefore infer that TOCI is not only useful in introducing new surface oxides, but the generated oxides can be patterned by adopting known-fractal evolution theories.

Similar processes, while highly stochastic, have been modelled through molecular dynamics experiments following diffusion-limited aggregation mechanism.[14] The formation of these dendritic looking structures depends on surface and

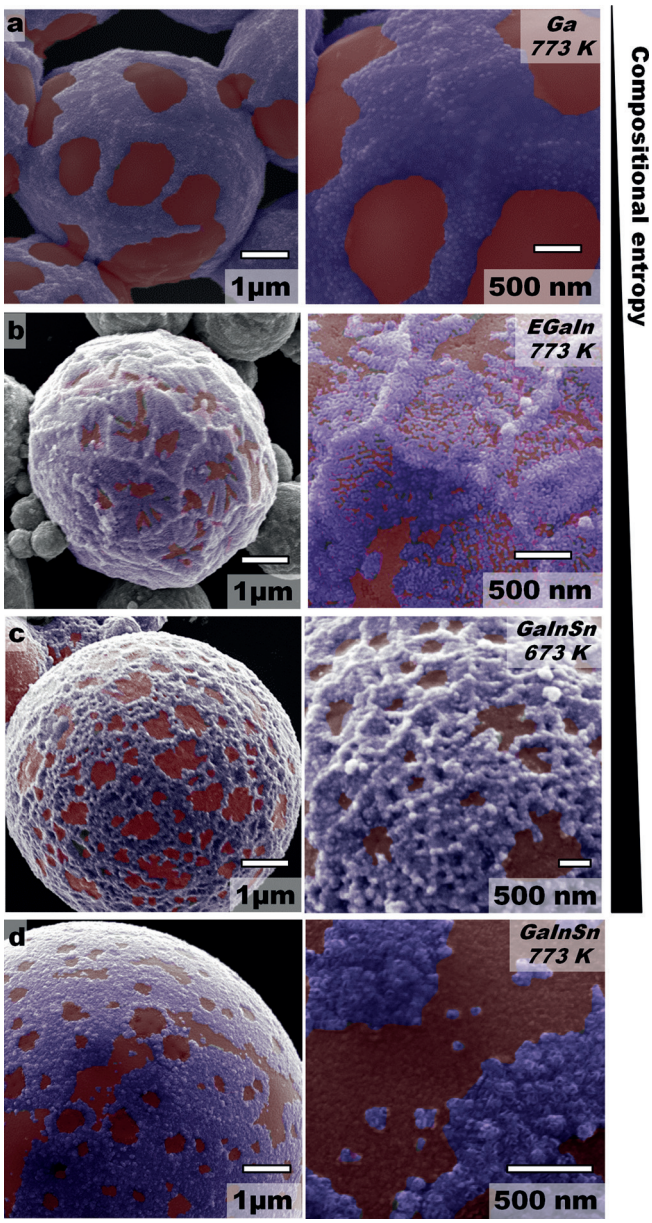

Figure 4. Micrographs of particles treated at intermediate temperatures: a) unary gallium at 773 K ($t=0$), b) EGaIn at 773 K ($t=0$), c) galinstan at 673 K (t isothermal = 15 min), d) 773 K ($t=0$). False colomicrographring is done to highlight surface features from the smooth oxide.

adsorbed particle interaction, with aggregation of formed features dependent on particle–particle interaction. In TOCI, the native surface oxide acts as the plane to which the oxide grows whilst oxygen is the adsorbate that eventually forms the surface oxide. Langmuir adsorption theory describes the probability of oxygen adsorption on the surface to be dependent on the adsorption/desorption ratio.[15] The probability of this event to occur increases as larger area of oxidized surface forms, which subsequently acts as an oxygen capture zone. Pure gallium forms larger aggregated oxide islands due to unrestricted gallium–oxygen interactions. In the alloys, stoichiometry-dependent perturbation of the Ga–oxygen interaction occurs leading to reduced deposition of surface oxide. Adding more components into a system will also increase the sub-oxide layers underneath its passivating oxide, further disrupting diffusion to the surface and the oxidation process. We infer that these perturbations are responsible for the low-volume features on EGaIn and galinstan. We infer that increasing compositional entropy in an alloy system(s) dictates fractal patterns and volumetric deposition in TOCI.

Contrary to growth on flat surfaces that commonly has long branches with a known origin, curved surface displays shorter chains and higher periodicity. An infinitesimal (tangential) space on the surface of a high curvature spherical particle is considerably flat, and thus can act as the source or oxide capture zone for the oxide growth. There are, however, an infinite number of these infinitesimal flat surfaces around the whole surface, which results in high numbers of oxide growth origins. It is therefore not surprising that the patterns on these particles appear as sintered small particles.

Conclusion

In conclusion, we have demonstrated compositional inversion in a liquid ternary alloy and indirectly confirm interfacial enrichment with formation of passivating oxides. This process leads to thermal-oxidative composition inversion—rendering these "chameleon" surfaces. Inverse complementarity in surface and bulk composition in fully oxidized particles supports this inference. Tuning the processing temperature leads to size-tunable growth of either spherical particles or cilia-like nanowires on the surface of these particles. Exploiting the underlying TFO mechanism, plastic reconstruction in the liquid, and stoichiometric dependence of chemical reactions, fracture-guided deposition introduced a new fractal-based approach to surface nano-patterning. A combination of these two inferences should inspire design of "smart" alloy systems that evolve the surface patterns and their composition with temperature (or analogous stimuli) for application ranging from sensing[16] to catalysis.[5,17]

Experimental Section

Particle synthesis (Galinstan example): Particle synthesis procedure follows a method published previously.[7a] 100 mL of 5% (V/V) aqueous solution of glacial acetic acid was placed in Cuisinart® (SBC-1000FR) soup maker. 4 g of galinstan were placed in the solution and sheared at a speed of 13000 rpm for 20 minutes. The resulting suspension was allowed to settle for 5 minutes, decanted and the resulting sediment was diluted in ethanol (4 × 100 mL) after which it was stored in ethanol.

Particle heat treatment: The particles were heat treated using Thermogravimetric Analyzer (TA Instruments Q50 TGA) instrument. Undoped silicon wafers were cleaned using ethanol and then dried using a stream of ultrahigh-purity Nitrogen Gas. The particles were then drop cast on the clean silicon wafer and the solvent was allowed to evaporate in an oven at 60 °C for 1 min. The particles on the silicon wafer were then transferred to the TGA after being placed on a platinum pan. The heat treatment was carried in presence of air, air gas flow rate was set at 60 mL min^{-1} and ramp rate of 10 °C min^{-1}.

Characterization: The as-synthesized particles were imaged using scanning electron microscopy (FEI-SEM Quanta 250). Prior to

imaging, all heat-treated particles were equilibrated to ambient conditions and mounted on a flat SEM stub (Ted Pella, Inc.) using a copper tape. An accelerating voltage of 10 kV and working distance of ca. 10 mm was used for the imaging. Images were obtained using an Everhart–Thornley secondary electron detector. Elemental analysis was carried out using Energy Dispersive X-ray Spectrometer (EDS). Accelerating voltage of 15 kV and a working distance of 10 mm was used to attain high spectral resolution. Maps were taken at 1024 pixel resolution with 500 μs dwell time.

Focused Ion Beam (FIB) Machining and Preparation: Heat treated sample was mounted on a flat SEM stub (Ted Pella, Inc.) on which copper tape had been laid, carbon paint was added on the edges of the sample for better conductivity. Sample was prepared using a FEI Helios NanoLab G3. Eucentric height of the system was established as 4 mm and was used for milling and imaging. Machining was carried out at 16 kV on the Ion column using Si-α beam. The machining was performed at 52 degrees tilt, so that the surface was perpendicular with respect to the ion beam column axis. Imaging of cut sample was done at 3 kV using an Everhart–Thornley secondary electron detector. The sample was then rotated to face the EDS take-off tube for elemental mapping. Spectra were taken at 25 kV for all milled samples.

Acknowledgements

This work was supported by startup funds from Iowa State University and a Black & Veatch faculty fellowship to M.T.

Conflict of interest

The authors declare no conflict of interest.

Keywords: composition inversion · interfaces · liquid metal · nano-scale · surface patterning

How to cite: *Angew. Chem. Int. Ed.* **2020**, *59*, 352–357
Angew. Chem. **2020**, *132*, 360–365

[1] E. Y. Bormashenko, *Wetting of Real Surfaces*, *Vol. 19*, de Gruyter, Berlin, **2013**.

[2] a) J. Cutinho, B. S. Chang, S. Oyola-Reynoso, J. Chen, S. S. Akhter, I. D. Tevis, N. J. Bello, A. Martin, M. C. Foster, M. M. Thuo, *ACS Nano* **2018**, *12*, 4744–4753; b) S. Oyola-Reynoso, I. D. Tevis, J. Chen, B. S. Chang, S. Çinar, J. F. Bloch, M. M. Thuo, *J. Mater. Chem. A* **2016**, *4*, 14729–14738; c) L. Cademartiri, M. M. Thuo, C. A. Nijhuis, W. F. Reus, S. Tricard, J. R. Barber, R. N. S. Sodhi, P. Brodersen, C. Kim, R. C. Chiechi, G. M. Whitesides, *J. Phys. Chem. C* **2012**, *116*, 10848–10860; d) R. N. S. Sodhi, P. Brodersen, L. Cademartiri, M. M. Thuo, C. A. Nijhuis, *Surf. Interface Anal.* **2017**, *49*, 1309–1315; e) R. Alert, J. Casademunt, P. Tierno, *Phys. Rev. Lett.* **2014**, *113*, 198301; f) R. Alert, P. Tierno, J. Casademunt, *Nat. Commun.* **2016**, *7*, 13067.

[3] a) R. C. Chiechi, E. A. Weiss, M. D. Dickey, G. M. Whitesides, *Angew. Chem. Int. Ed.* **2008**, *47*, 142; *Angew. Chem.* **2008**, *120*, 148; b) M. D. Dickey, *Adv. Mater.* **2017**, *29*, 1606425; c) M. D. Dickey, *ACS Appl. Mater. Interfaces* **2014**, *6*, 18369–18379.

[4] a) H. Over, A. P. Seitsonen, *Science* **2002**, *297*, 2003–2005; b) G. Y. Lai, *High temperature corrosion of engineering alloys*, American Society for Metals, Metals Park, **1990**; c) Q. Xu, N. Oudalov, Q. Guo, H. M. Jaeger, E. Brown, *Phys. Fluids* **2012**, *24*, 063101; d) C. M. Miller, I. E. Anderson, J. F. Smith, *J. Electron. Mater.* **1994**, *23*, 595–601; e) K. N. Reeve, J. R. Holaday, S. M. Choquette, I. E. Anderson, C. A. Handwerker, *J. Phase Equilib. Diffus.* **2016**, *37*, 369–386.

[5] D. Esrafilzadeh, A. Zavabeti, R. Jalili, P. Atkin, J. Choi, B. J. Carey, R. Brkljača, A. P. O'Mullane, M. D. Dickey, D. L. Officer, D. R. MacFarlane, T. Daeneke, K. Kalantar-Zadeh, *Nat. Commun.* **2019**, *10*, 865.

[6] D. Wang, X. Wang, Z. Li, M. Chi, Y. Li, Y. Liu, Y. Yin, *ACS Nano* **2018**, *12*, 10949–10956.

[7] a) I. D. Tevis, L. B. Newcomb, M. Thuo, *Langmuir* **2014**, *30*, 14308; b) S. Çınar, I. D. Tevis, J. Chen, M. Thuo, *Sci. Rep.* **2016**, *6*, 21864.

[8] a) Z. J. Farrell, C. Tabor, *Langmuir* **2018**, *34*, 234–240; b) H.-J. Butt, K. Graf, M. Kappl, *Physics and Chemistry of Interfaces*, 3rd ed., Wiley-VCH, Weinheim, **2013**.

[9] a) S. R. J. Saunders, M. Monteiro, F. Rizzo, *Prog. Mater. Sci.* **2008**, *53*, 775–837; b) N. Cabrera, N. F. Mott, *Rep. Prog. Phys.* **1949**, *12*, 163–184; c) L. L. Wang, D. D. Johnson, *J. Am. Chem. Soc.* **2009**, *131*, 14023–14029.

[10] a) M. J. Regan, H. Tostmann, P. S. Pershan, O. M. Magnussen, E. DiMasi, B. M. Ocko, M. Deutsch, *Phys. Rev. B* **1997**, *55*, 10786–10790; b) H. Tostmann, E. Dimasi, B. M. Ocko, M. Deutsch, P. S. Pershan, *J. Non-Cryst. Solids* **1999**, *250*, 182–190; c) M. Dumke, T. Tombrello, R. Weller, R. Housley, E. Cirlin, *Surf. Sci.* **1983**, *124*, 407–422.

[11] J. T. Law, *J. Phys. Chem.* **1957**, *61*, 1200–1205.

[12] S. Oyola-Reynoso, J. Chen, B. S. Chang, J.-F. Bloch, M. M. Thuo, *RSC Adv.* **2016**, *6*, 82233–82237.

[13] a) J. M. Chabala, *Phys. Rev. B* **1992**, *46*, 11346–11357; b) J. Dachs, J. M. Bayona, *Environ. Sci. Technol.* **1997**, *31*, 2754–2760; c) G. Zhou, J. C. Yang, *Appl. Surf. Sci.* **2004**, *222*, 357–364; d) L. Chen, J. Xu, P. Fleming, J. D. Holmes, M. A. Morris, *J. Phys. Chem. C* **2008**, *112*, 14286–14291.

[14] a) P. Meakin, *Phys. Rev. A* **1983**, *27*, 1495–1507; b) T. A. Witten, L. M. Sander, *Phys. Rev. Lett.* **1981**, *47*, 1400–1403.

[15] a) I. Langmuir, *J. Am. Chem. Soc.* **1918**, *40*, 1361–1403; b) J. M. Watson, G. S. Zhang, P. A. Payne, *J. Membr. Sci.* **1992**, *73*, 55–71.

[16] a) X. Li, C. Zhao, X. Liu, *Microsyst. Nanoeng.* **2015**, *1*, 15014; b) P. Song, Y.-H. Wang, X. Liu, *Flexible Printed Electron.* **2017**, *2*, 034001.

[17] a) W. Zhang, B. S. Naidu, J. Z. Ou, A. P. O'Mullane, A. F. Chrimes, B. J. Carey, Y. Wang, S.-Y. Tang, V. Sivan, A. Mitchell, S. K. Bhargava, K. Kalantar-Zadeh, *ACS Appl. Mater. Interfaces* **2015**, *7*, 1943; b) Q. Yue, Y. Zhang, C. Wang, X. Wang, Z. Sun, X.-F. Hou, D. Zhao, Y. Deng, *J. Mater. Chem. A* **2015**, *3*, 4586–4594; c) Q. Yue, Y. Zhang, Y. Jiang, J. Li, H. Zhang, C. Yu, A. A. Elzatahry, A. Alghamdi, Y. Deng, D. Zhao, *J. Am. Chem. Soc.* **2017**, *139*, 4954–4961; d) J. Tang, Z. Huo, S. Brittman, H. Gao, P. Yang, *Nat. Nanotechnol.* **2011**, *6*, 568–572.

Manuscript received: October 2, 2019
Revised manuscript received: November 6, 2019
Accepted manuscript online: November 19, 2019
Version of record online: December 2, 2019

